GSA Data Repository item 2019371

Constraining the maximum depth of brittle deformation at slow and ultraslow spreading ridges using micro-seismicity

Ingo Grevemeyer[1], Nicholas W. Hayman[2], Dietrich Lange[1], Christine Peirce[3], Cord Papenberg[1], Harm J. A. Van Avendonk[2], Florian Schmid[1], Laura Gomez de La Pena[1], and Anke Dannowski[1]

[1]*GEOMAR Helmholtz Centre of Ocean Research, Wischhofstr. 1-3, 24148 Kiel, Germany*

[2]*Institute for Geophysics, Jackson School of Geosciences, University of Texas at Austin, 10100 Burnet Road, Austin, Texas 78758, USA*

[3]*Department of Earth Sciences, University of Durham, South Road, Durham DH1 3LE, UK*

METHODS

I. Earthquake location procedure for the Mid-Cayman Spreading Center (MCSC) dataset

The quality of focal parameters of local earthquakes is inherently associated with a number of aspects, including the total number of phase readings, the number of P-wave arrivals, the number of S-wave arrivals, the distance of each station from the epicenter, and the azimuthal distribution of stations. In addition, a correct earthquake location requires a correct velocity structure, which is, unfortunately, never exactly known and results in a trade-off between velocity model and earthquake parameters. However, seismic refraction data from the MCSC (Van Avendonk et al., 2017) provides a P-wave velocity structure constraint, while S-wave velocity can be approximated from the Vp/Vs ratio (Fig. S1) using a Wadati plot.

For location, we use the non-linear oct-tree search algorithm of the NonLinLoc program package (Lomax et al., 2000). Travel times in the model are calculated using the finite-difference solution to the Eikonal equation (Podvin and Lecomte, 1991). The oct-tree algorithm provides more reliable information on location uncertainties than linearized inversions by exploring the probability density functions (PDF) of each individual event over the search area. The maximum likelihood location is chosen as the preferred location and for each event NonLinLoc estimates a 3D error ellipsoid (68% confidence) from the PDF scatter

samples. Furthermore, 3D effects are compensated by iterative calculation of station correction terms until the average RMS misfit yields a minimum.

We detected earthquakes automatically in the continuous time series using a short-term-average to long-term-average ratio (STA/LTA) trigger algorithm, surveying vertical components from 23 OBS recording successfully micro-earthquakes in the Cayman Trough (Grevemeyer et al., 2015). An event was considered to be an earthquake when six or more stations triggered coincidently. We detected and located 310 earthquakes that were registered into a SEISAN database (Havskov and Ottemöller, 2005). P- and S-wave arrival onset times were hand-picked. In total, we were able to locate about 300 local earthquakes. Each onset has been classified into one of four categories, having picking errors of ±0.05 s, ±0.1 s, ±0.15 s and ±0.2 s, respectively. In general, the P-wave phase-pick error is of the order of ±0.05-0.1 s, while most S-wave phase-pick errors were larger at between ±0.1-0.2 s.

Following the approach of Tilmann et al. (2008), we used hydrophone traces for the calculation of moment magnitudes M_w. Thus, we removed the nominal response and multiplied the corrected hydrophone trace by the sound velocity (1.5 km/s) and the density of water (1000 kg/m^3). The resulting trace approximates the displacement for a vertically incident wave and zero impedance contrast between seafloor and water. This approximation is reasonable, since velocities and densities of the uppermost sediments are comparable to that in water and cause earthquake arrivals to have steep ray paths below the station. The moment magnitudes were then calculated by applying the standard method and code of Ottemöller and Havskov (2003), which searches for the combination of seismic moment (M_0) and corner frequency (f_0) that fits the observed spectra. Note that the moment release and seismicity rate at the MCSC are significantly lower when compared to other oceanic core complexes (e.g., deMartin et al., 2007; Grevemeyer et al., 2013; Parnell-Turner et al., 2017).

To provide a hypocenter with good precision, eight or more travel time arrivals, including one S-onset and one arrival time within a focal depth distance from the epicenter are required (Chatelain et al., 1980). Additionally, a correctly timed S-wave arrival recorded within 1.4 focal depth distance from the epicenter is also required to improve focal depth estimation (Gomberg et al., 1990). We, therefore, use as an initial criterion that at least six OBSs should have recorded any earthquake to be processed. In addition, events should also occur within the network and hence have a station gap of <180°. In the case of our network, we have ~1900 phase readings for both P- and S-waves; thus, the criteria for S-wave arrivals are always met. With an instrument spacing of 5-7 km within the network (Fig. 1), we have a dense station separation and coverage of the median valley, allowing us to locate events at high precision and revealing that most events occur at crustal level or within the uppermost mantle at focal depths of <10 km below seafloor. Similar features are found at other mid-ocean ridge settings (e.g. deMartin et al., 2007; Grevemeyer et al., 2013).

In order to evaluate focal parameters, we used an iterative location procedure. Initially, only Vp structure and P-onset times were used. In a second step, we included S-waves, assessing S-wave velocity from Vp/Vs ratio (Fig. S1). Both approaches provide matching epicentral locations and focal depths for the MCSC dataset. Gaussian distribution of residuum suggests that appropriate station terms have been applied (Fig. S2). Projecting the earthquakes on to

the seismic profile of Van Avendonk et al. (2017), shot along the median valley, indicates very little seismic activity in rocks with velocities of <6 km/s, with the majority of the seismicity occurring at velocities of >6.5 km/s (Fig. S3). However, hardly any earthquakes occur at >12 km, with all well-located earthquakes having a gap of <180° occurring predominantly between 2 km and ~10 km below seafloor.

II. Earthquake location procedure for the Southwest Indian Ridge (SWIR)

Our new perspective on the SWIR was based on the data catalog of Schmid and Schlindwein (2016), which was obtained by recording micro-earthquakes at the oblique super segment of the SWIR (Fig. S4). Thus, we do not perform any analysis of waveform data. We selected only events with at least eight travel time arrivals, including one S-onset and one arrival time within the focal depth distance from the epicenter (Chatelain et al., 1980). The condition of one correctly timed S-wave arrival recorded within 1.4 focal depth distance from the epicenter (Gomberg et al., 1990) was not always met for the SWIR dataset as the station separation of 20 km to 40 km limits constraint on focal depths shallower than <10-20 km. However, between early December 2012 to 31st May 2013, eight OBSs provide a large number of local earthquakes that were recorded at six or more OBSs, including at least one S-arrival time and having a station gap <180°, resulting in 470 micro-earthquakes.

We follow the same location procedure described above. Note that we tested different velocity models (e.g. oceanic crust versus serpentinized mantle), but they all provided similar focal depths within the context of the data errors.

First, we located events using P-onsets only. The resulting depth distribution deviates significantly from Schmid and Schlindwein (2016), which showed only a small number of micro-earthquakes in the uppermost 5-10 km of the lithosphere, with most events clustering at ~10 km to 30 km depth (Fig. S5a). Our approach instead suggests micro-earthquakes occurring close to the seafloor and extending to ~17 km depth, with a very small number of events occurring at ~20-30 km depth (Fig. S5b).

Adding S-onsets, initial relocations show a wide range of focal depths (after two iterations of updated station terms and using a limited search grid), including a large number of deeper earthquakes (Fig. S5c). The average misfit is poorer, doubling from ~0.05 s for P-onsets only to 0.12 s for both P- and S-waves. The non-Gaussian distribution of S-residuals is also poorer (Fig. S6). In general, the RMS misfit may be a reasonably unreliable measure for the quality of earthquake focal parameters, as larger numbers of arrival times often cause larger RMS misfit. However, the strong discrepancy between locations derived from P-waves only and P- and S-waves together, and the large number of poor S-arrival times, may indicate some bias in S-wave velocity structure.

Wadati's relationship between S-P and origin time (Fig. S7a) provides further evidence for a bias in S-onset times, shown by a very scattered distribution. The resulting distribution shows a number of different trends, one roughly indicating a constant Vp/Vs ratio of ~1.8 and trends offset by 1 to 2 s, indicating a strong delay of S-onset at a number of stations. Appraisal of S-delays for individual stations suggests that, with the exception of OBS02 and OBS03, all

other OBSs show S-delays ranging from ~0.4 s to ~2 s (Fig. S8), while P-delay times are <0.05 s. An iterative update of station delays using NonLinLoc removes, after 11 iterations, this scatter (Fig. S7b) and provides a Gaussian distribution of residuals (Figs S6c and S6d). An even better fit is achieved when calculating station delays based on the Wadati diagrams as shown in Fig. S8 (cf. Fig. S7c). However, relying on the corrections provided by the iterative update of station terms obtained from NonLinLoc, the average RMS misfit improves from >0.2 s to <0.09 s (Fig. S9). The resulting depth distribution becomes rather more limited, providing micro-earthquakes between ~1 km to ~17 km depth below seafloor (Figs. S5d and Fig. 2).

We believe that the large delay of S-waves is caused by unconsolidated sediments that Schmid and Sclindwein (2016) report, which cover the ridge axis locally by at least 150 m. A 200 m-thick section of slow Vs sediment could account for an S-delay of 1 s, assuming an S-wave velocity of ~200 m/s. Such low S-wave velocities have been reported for mid-ocean ridge settings elsewhere (e.g. Essen et al., 1998). Assuming that mass wasting processes may have accumulated sediment locally, up to ~400 m of sediment could explain the observed delay times.

REFERENCES CITED

Chatelain, J.L., Roecker, S.W., Hatzfeld, D., and Molnar, P., 1980, Microearthquake seismicity and fault plane solutions in the Hindu Kush region and their tectonic implications: J. Geophys. Res., v. 85, p. 1365-1387.

deMartin, B.J., Sohn, R.A., Canales, J.P., Humphris, S.E., 2007, Kinematics and geometry of active detachment faulting beneath the Trans-Atlantic Geotraverse (TAG) hydrothermal field on the Mid-Atlantic Ridge: Geology, v. 35, p. 711–714, doi:10.1130/G23718A.1.

Essen, H.-H., Grevemeyer, I., Herber, R., and Weigel, W., 1998, Shear wave velocity in marine sediments on young oceanic crust: constraints from dispersion analysis of Scholte waves: Geophys. J. Int., v. 132, p. 227-234.

Gomberg, J.S., Shedlock,K.M., and Roecker, S.W., 1990, The effect of S-Wave arrival times on the accuracy of hypocenter estimation: Bull. Seism. Soc. Am., v. 80, p. 1605-1628.

Grevemeyer, I., Reston, T.J., and Moeller, S., 2013, Microseismcity of the Mid-Atlantic Ridge at 7°–8°15′S and at the Logatchev Massif oceanic core complex at 14°40′N–14°50′N: Geochem. Geophys. Geosyst., v. 14, p. 3532–3554, doi:10.1002/ggge.20197.

Grevemeyer, I., Dannowski, A., Hayman, N.W., Peirce, C., and van Avendonk, H., (2016) CAYSEIS: magma-starved oceanic crustal accretion and transform margin formation in the Cayman Trough revealed by seismic and seismological data – Cruise No. M115 – April 1 – April 28, 2015 – Kingston (Jamaica) – Pointe-à-Pitre (Guadeloupe). METEOR-Berichte, M115, 56 pp., DFG-Senatskommission für Ozeanographie, doi:10.2312/cr_m115

Havskov, J., and Ottemöller,L., 2000, SEISAN earthquake analysis software, Seismol. Res. Lett., v. 70, p. 532–534.

Lomax, A., Virieux, A. J., Volant, P., and Berge, C., 2000, Probabilistic earthquake location in 3D and layered models: Introduction of a Metropolis-Gibbs method and comparison with linear locations, in Advances in Seismic Event Location, Thurber, C. H. and Rabinowitz, eds., N., Kluwer, Amsterdam, p. 101-134.

Ottemöller, L., and Havskov, J., 2003. Moment magnitude determination for local and regional earthquakes based on source spectra: Bul. seism. Soc. Am., v. 93, p. 203–214.

Parnell-Turner, R., Sohn, R.A., Peirce, C., Reston, T.J., Macleod, C.J., Searle, R.C., and Simão, N.M., 2017, Oceanic detachment faults generate compression in extension: Geology, v. 45, p. 923-926 doi:10.1130/G39232.1.

Podvin, P., and Lecomte, L., 1991. Finite difference computation of traveltimes in very contrasted velocity models: a massively parallel approach and its associated tools, Geophys. J. Int., v. 105, p. 271–284. doi:10.1111/j.1365-246X.1991.tb03461.x.

Schmid, F., and Schlindwein, V., 2016, Microearthquake activity, lithospheric structure and deformation modes at an amagmatic ultraslow spreading Southwest Indian Ridge segment: Geochem., Geophys., Geosyst., v. 17, p. 2905–2921, doi:10.1002/2016gc006271.

Tilmann, F.J., Grevemeyer, I., Flueh, E.R., Dahm, T., and Goßler, J., 2008, Seismicity in the outer rise offshore southern Chile: indication of fluid effects in crust and mantle: Earth Planet. Sci. Lett., v. 269, p. 41–55.

Van Avendonk, H.J.A., Hayman, N.W., Harding, J.L., Grevemeyer, I., Peirce, C., and Dannowski, A., 2017, Seismic structure and segmentation of the axial valley of the Mid-Cayman Spreading Center, Geochem. Geophys. Geosyst., 18, 2149–2161, doi:10.1002/2017GC006873.

Table S1: Focal mechanisms shown in Fig. 1. Depth is in km; Mag. is moment magnitude Mw; focal mechanism as strike, dip, and rake.

Year	Date	Time	Latitude	Longitude	Depth	Mag.	Focal mechanism		
2015	0403	2248	18.2359	-81.7433	6.0	1.8	176.41	41.03	-74.66
2015	0404	0137	18.3531	-81.7342	6.2	1.8	341.34	75.06	-84.82
2015	0404	1220	18.3302	-81.7387	2.0	1.9	008.23	60.50	-78.49
2015	0406	0119	18.3302	-81.7222	3.8	1.8	069.05	30.00	90.00
2015	0407	0143	18.4510	-81.7900	5.0	2.3	219.46	10.00	-90.00
2015	0407	0458	18.4767	-81.7094	3.2	2.1	316.78	27.99	43.22
2015	0410	913	18.3952	-81.7304	1.7	2.1	212.91	43.96	-60.48
2015	0411	1746	18.4080	-81.7103	7.4	2.9	353.50	39.22	49.96
2015	0411	2231	18.3833	-81.7350	4.3	2.2	348.99	27.99	43.22
2015	0412	0308	18.3988	-81.7707	8.1	2.2	338.00	48.44	30.79
2015	0412	2056	18.6524	-81.8119	5.5	2.9	255.66	50.18	-4.18
2015	0416	0219	18.4213	-81.7300	8.3	3.8	131.19	54.60	29.84
2015	0418	1716	18.3531	-81.6444	7.0	2.8	262.66	41.03	-74.66
2015	0418	2213	18.2414	-81.7433	4.1	2.8	153.33	10.00	00.00

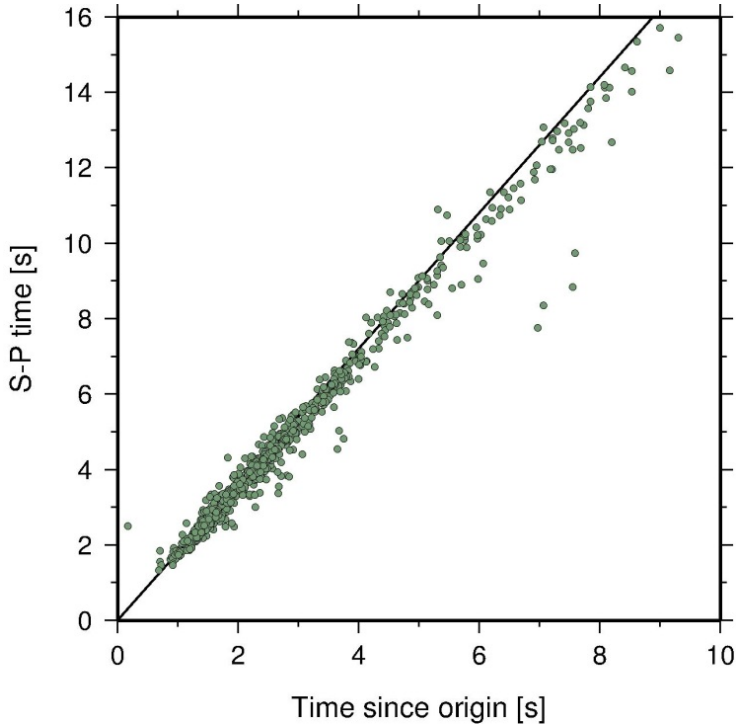

Figure S1. Wadati diagram of P-onset versus S-P time, yielding Vp/Vs ratio for the MCSC.

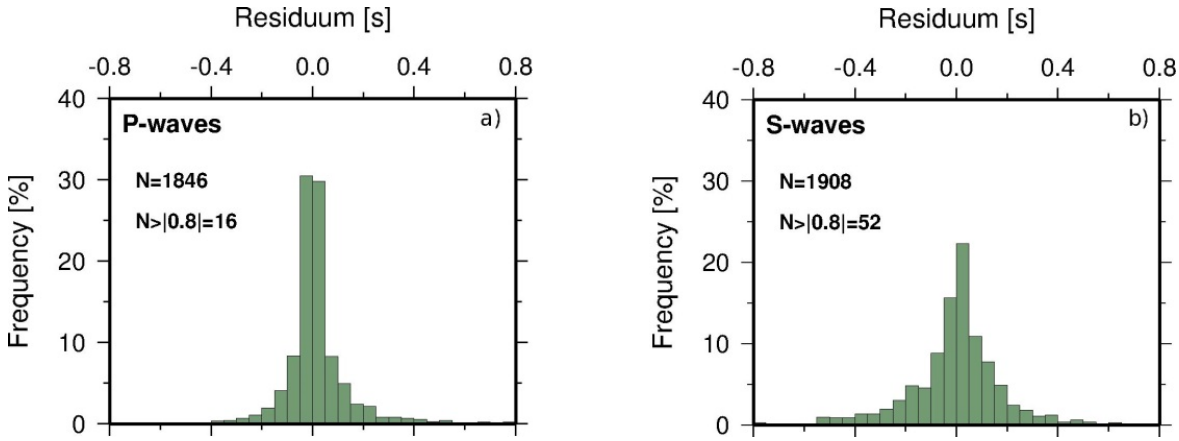

Figure S2. a) P-wave and b) S-wave residuals of the location procedure.

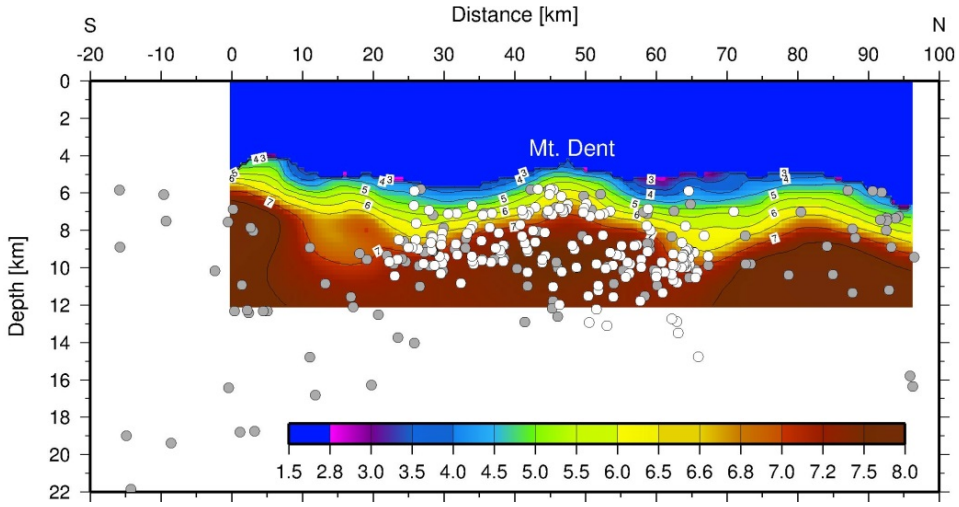

Figure S3. Micro-seismicity from the MCSC projected on to the velocity model of Van Avendonk et al. (2017). Note event depth is below sea-surface and not below seafloor e.g. as in Fig. 1 and in the histograms provided in other figures. White dots are events with a station gap <180°. Gray dots show events with larger gaps.

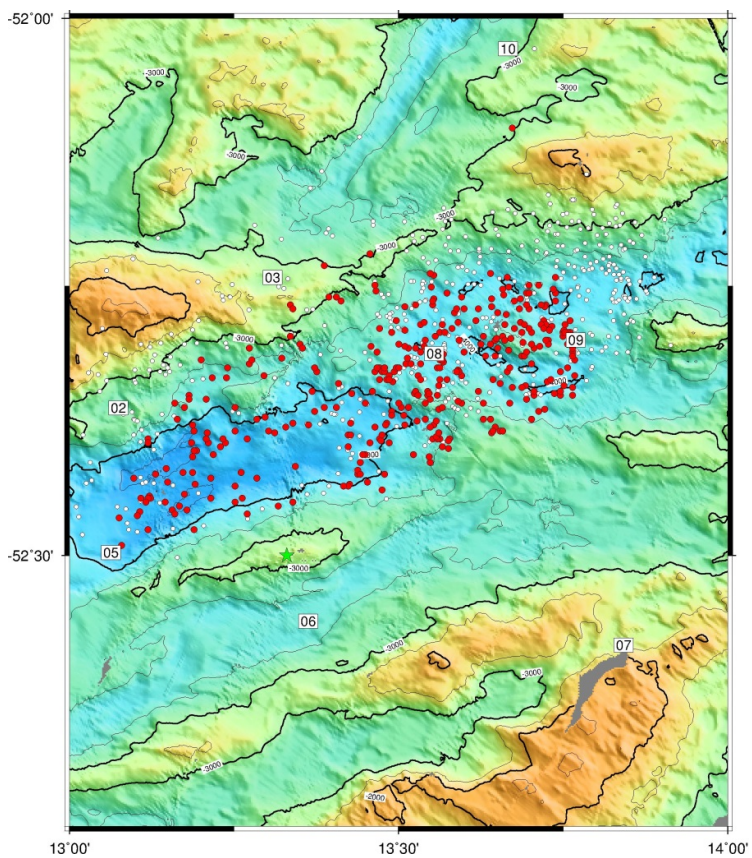

Figure S4. Location map of the micro-seismicity study at the Southwest Indian Ridge (Schmid and Schlindwein, 2016) with epicenters of re-located events (red dots are earthquakes with station gap <180° observed at six or more stations; white dots are events with larger gap). Same color scale as Fig. 1. Numbers (02, 03, 05, 06, 07, 08, 09, 10) indicate the locations of OBSs.

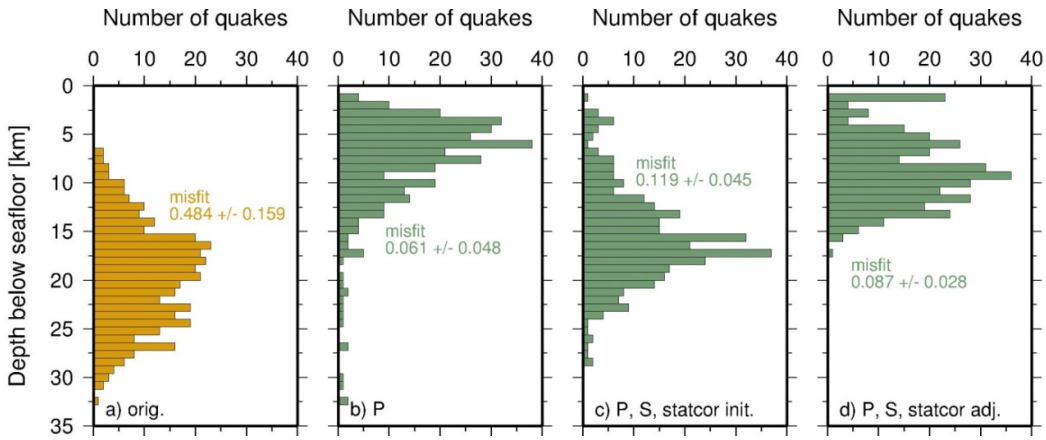

Figure S5. Histograms of the depth distribution of micro-earthquakes at the SWIR obtained from our re-analysis of the Schmid and Schlindwein (2016) catalog. a) Original distribution. b) Depth distribution by P-waves only. c) Depth distribution using a limited search grid for LonLinLoc. d) Final depth distribution after application of recalculated station corrections.

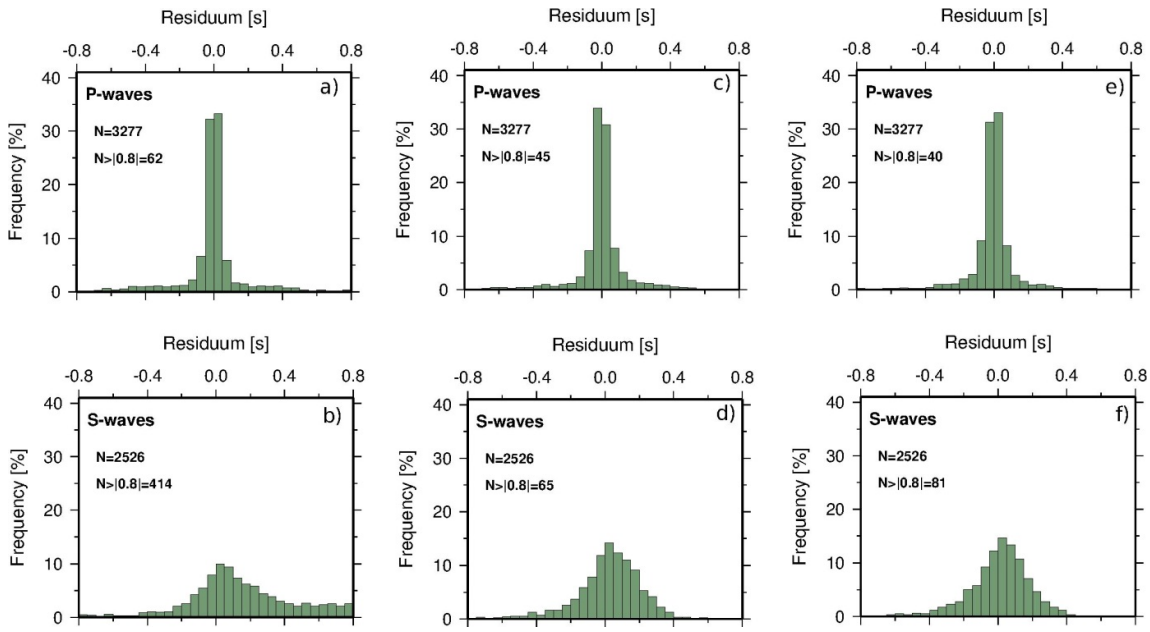

Figure S6. P-wave and S-wave residuals from the location procedure. a) and b) Residuals after two iterations of updated station terms and using a limited search grid (for histogram shown in Fig. S5b). c) and d) Residuals after 11 iterations of updated station corrections and extended search grid (for histogram shown in Fig. S5c). e) and f) Residuals for an inversion where updated station corrections were used to remove the bias observed in individual Wadati diagrams of Fig. S8.

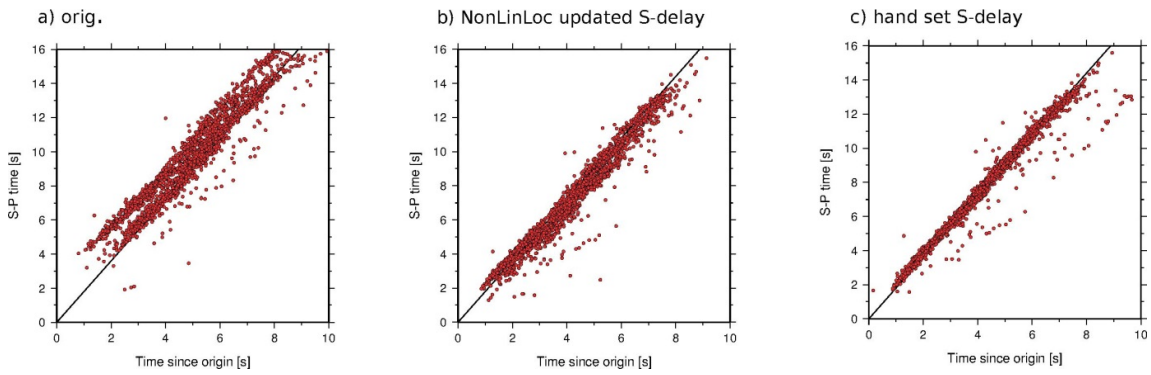

Figure S7. Wadati diagrams of P-onset versus S-P time for the SWIR dataset. a) Wadati diagram calculated from the original data catalog. b) Wadati diagram after iterative update of station corrections. c) Wadati diagram with station delays calculated by removing the bias observed in individual Wadati diagrams shown in Fig. S8.

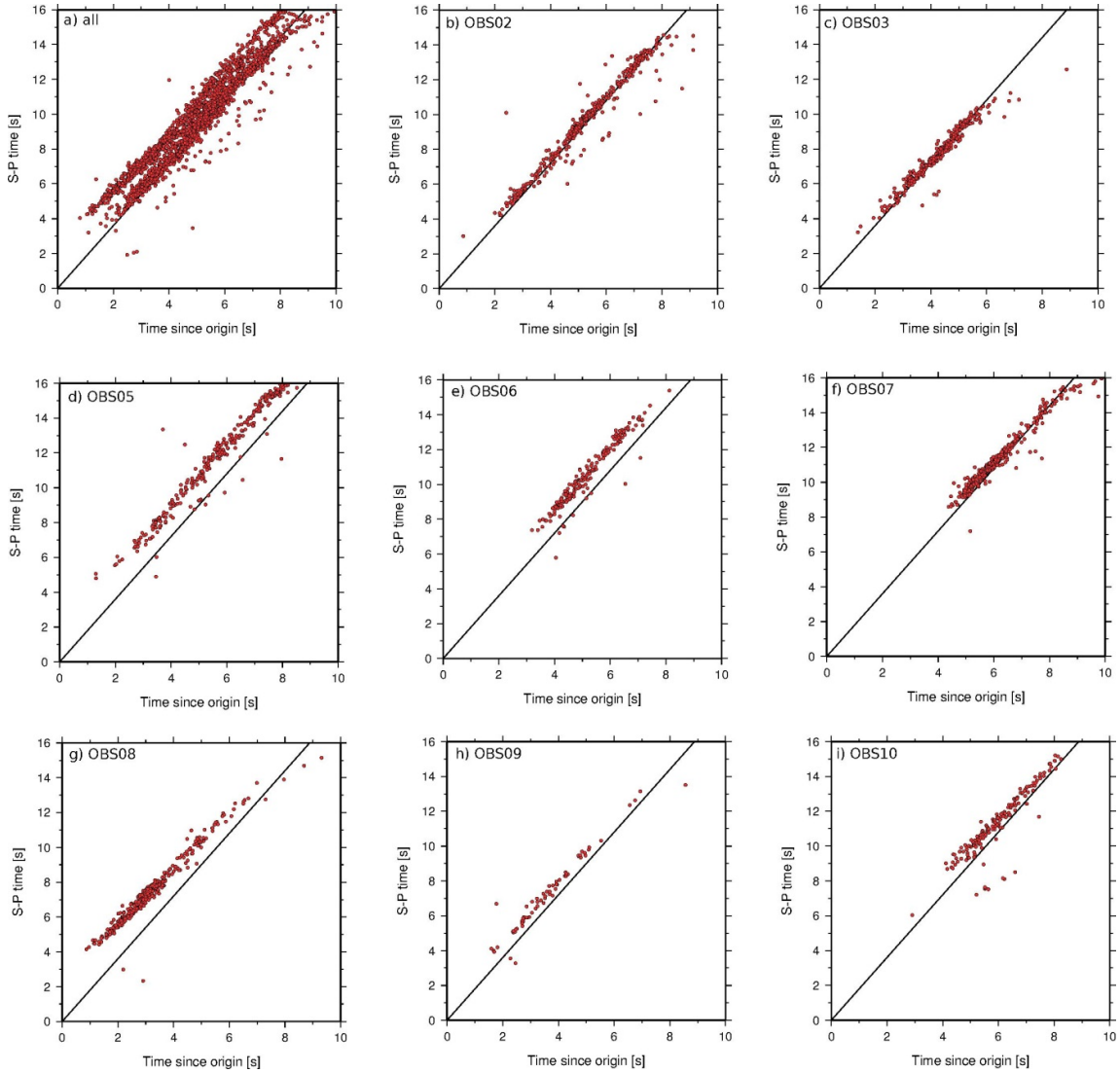

Figure S8. Wadati diagram of the original data set (a) together with those for individual stations (b-i) shown in Fig. S4 and used in this study.

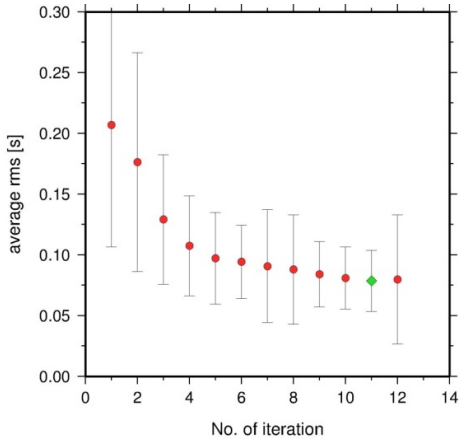

Figure S9. Average RMS residuals plotted as a function of iterations run to calculate station corrections.